JOURNAL OF GUIDANCE, CONTROL, AND DYNAMICS
Vol. 27, No. 4, July–August 2004

Multibody Dynamics of Parachute and Balloon Flight Systems for Planetary Exploration

Marco B. Quadrelli,* Jonathan M. Cameron,† and Viktor Kerzhanovich‡
Jet Propulsion Laboratory, California Institute of Technology, Pasadena, California 91109-8099

Some of the models and simulation capabilities developed for analyzing parachute and balloon-assisted deployment of sensor packages within the Mars Aerobot Validation Program at Jet Propulsion Laboratory, California Institute of Technology, are described. Different events occurring during the deployment of the system are considered. First, the effect of the detachment of the top parachute and the inflation of the balloon on the system stability are analyzed. Second, constitutive models of the ripstitch (shock alleviation device) are developed that compare well with experimental data. Third, the balloon is assumed to have reached a floating altitude, and the system response when a hinged camera is commanded to track an inertially fixed point on the surface of the planet is observed while perturbations in the form of wind gusts act on the system. These models and simulations have been motivated by the need to predict and validate flight-train stability behavior on deployment in support of flight tests.

I. Introduction

THE Mars Balloon Validation Program (MABVAP) was initiated in August 1997 to develop and validate key technologies needed for aerobot missions on Mars. The sequence of steps involved in the tests done during the MABVAP program is as follows: The balloon with all associated systems is packed inside the aeroshell. 1) First, the balloon enters into the atmosphere. 2) Then, the aftshell and the heatshield separate and the parachute deploys. 3) A few seconds after reaching the terminal velocity, the balloon container opens and the balloon deploys with the suspended inflation system and payload. 4) Some moments after start of the inflation, the parachute releases, and the balloon with the inflation system continues to descend. 5) The inflation system is released when the inflation process is completed and the balloon and the parachute reach sufficient separation. 6) The balloon starts to ascend to the float altitude. Because the density of the Martian atmosphere is so low, the deployment starts at about 10 km above the average surface; the separation of the inflation system, the lowest point, should be 1–2 km above the real surface. The whole process should be completed in 200–300 s. Figure 1, taken from Ref. 1, shows photographs of deployment and inflation of a 3-m-diam Mylar balloon. The test validated the concept of the bottom inflation for the tropospheric deployment. Figure 2 shows the sequence of the adopted stratospheric aerial deployment and inflation concept.

During the deployment process, several considerations come into play: mitigation of forces on the balloon during deployment, a safe deployment process that does not tear the balloon, and the avoidance of subsequent instabilities of the balloon, including the helium gas bulb propagation inside the balloon. Other key design issues include the necessity for a reefing mechanism for ensuring stable and predictable inflation of the balloon and the choice between top and bottom inflation. The intent of the models and simulation analysis described in this paper is to determine the onset of dynamic oscillatory instability (presumably attributed to von Karman vortex shedding) of the balloon as a function of design parameters such as parachute diameters and riser length, balloon diameter, balloon–gondola tether length, and gondola mass and inertia. The simulation models described in this paper have been used to model the tests described in further detail in Refs. 1–3. Previous related work has focused on aerostat performance, infrared balloon thermal dynamics, and alternative precursor concepts for planetary balloon technology (see Refs. 4–7). The novelty of the deployment concept under consideration is that it focuses on the critical deployment and inflation technologies required to deploy balloons on other planets.

First, the equations of motion of the complex parachute–balloon–gondola flight train are described. The tethers between the parachute and the balloon, and between the balloon and the gondola, are also modeled. Second, using the models just described, we analyze the descent of the system when the parachute is suddenly detached and the balloon inflates, with the intent of observing the stability of the residual gondola oscillations and identifying possible failure modes. Third, we describe the development of the constitutive models of shock alleviation devices (ripstitch) used in the flight train, which agree well with experimental data. The ripstitch is a 20-m-long webbing folded in the middle and stitched with certain rows of thread, and it was used as a deployment shock absorber. The number of rows of thread determines the device ripping force and the shock alleviation capability. Fourth, we analyze the pointing dynamics and control of an articulated payload mounted on a balloon-supported gondola. This was a separate analysis conducted to complete the study and develop models to be used for precision pointing from balloon-assisted planetary platforms. The analysis also verified the feasibility of tracking an inertially fixed point from a gimballed payload aboard a floating aerobot. The equations of motion and control laws are described, as are numerical results obtained for one of many different configurations that cover a domain in a parameter space defined in terms of wind gust profiles, tether lengths, balloon diameters, and gondola/camera inertia properties.

II. Physical Models of Balloon and Parachute Behavior

A. Assumptions

The assumptions of the model shown in Fig. 3 are described next. In Fig. 3, G denotes the gondola, P the parachute, B the balloon, C the camera, and T_1 and T_2 the tethers. W_i, $i = 1, 2, 3$, are the reaction wheels and P_i the tether points. The reference frames of interest are the inertial frame (or planet frame) and the gondola (or body-fixed) frame. The gondola is taken here to be the preferential body, contrary to common balloon dynamics usage that places the body frame at the balloon, because sensors and actuators are located on the

Presented as Paper 2001-2026 at the AIAA 16th Aerodynamic Decelerator Systems Conference, Boston, MA, 20–24 May 2001; received 7 June 2001; revision received 14 October 2003; accepted for publication 28 October 2003.

*Member of Technical Staff, Autonomy and Control Section, Mail Stop 198-326, 4800 Oak Grove Drive; marco@grover.jpl.nasa.gov. Senior Member AIAA.

†Member of Technical Staff, Autonomy and Control Section, 4800 Oak Grove Drive.

‡Member of Technical Staff, Avionic Systems Engineering Section, 4800 Oak Grove Drive.

gondola rather than on the balloon. The inertial coordinate frame N is denoted by the triad $\hat{\boldsymbol{F}}_n = (\boldsymbol{n}_1, \boldsymbol{n}_2, \boldsymbol{n}_3)$ and the gondola body frame G by $\hat{\boldsymbol{F}}_b = (\boldsymbol{b}_1, \boldsymbol{b}_2, \boldsymbol{b}_3)$. The translation dynamics are measured in N, whereas the rotation dynamics of the gondola, camera, and wheels are measured in G.

The translational dynamics of G are parameterized in terms of the linear velocity components of its center of mass $G+$ as ${}^N\boldsymbol{v}^{G+} = (\dot{x}, \dot{y}, \dot{z})\hat{\boldsymbol{F}}_n$ and the rotational dynamics as ${}^N\boldsymbol{\omega}^G = (\omega_1, \omega_2, \omega_3)\hat{\boldsymbol{F}}_b$. The translational dynamics of each tether point P_i are parameterized in terms of the linear velocity components of its center of mass as ${}^N\boldsymbol{v}^{P_i} = (\dot{x}_i, \dot{y}_i, \dot{z}_i)\hat{\boldsymbol{F}}_n$. The balloon center of mass has a velocity ${}^N\boldsymbol{v}^B = (\dot{x}_b, \dot{y}_b, \dot{z}_b)\hat{\boldsymbol{F}}_n$. The parachute center of mass has a velocity ${}^N\boldsymbol{v}^P = (\dot{x}_p, \dot{y}_p, \dot{z}_p)\hat{\boldsymbol{F}}_n$. The rotation dynamics of the ith wheel W_i are parameterized as ${}^G\boldsymbol{\omega}^{W_i} = \Omega_i \boldsymbol{a}_i$, where Ω_i is the spin rate of the wheel with respect to the gondola and $\boldsymbol{a}_i$ denotes the direction of the spin axis in $\boldsymbol{F}_b$. (Here, $\boldsymbol{a}_i = \boldsymbol{b}_i$.) The absolute angular velocity of the camera is ${}^N\boldsymbol{\omega}^C = {}^N\boldsymbol{\omega}^G + (\dot{\phi}s\theta, -\dot{\phi}c\theta, \dot{\theta})\hat{\boldsymbol{F}}_b$, where θ and ϕ denothe the camera gimbal angles and $s = \sin$ and $c = \cos$. The wind velocity vector is represented as $\boldsymbol{W}_{\text{wind}} = (U_x, U_y, U_z)\hat{\boldsymbol{F}}_n$. The accelerations of the points are denoted by $\boldsymbol{a}$, whereas the angular acceleration of frames is denoted by $\boldsymbol{\alpha}$. The attitude of the gondola is parameterized by a unit quaternion.

The camera P and the gondola G are modeled as rigid bodies. The tether connecting the gondola to the balloon is modeled as a viscoelastic continuum and discretized into N lumped masses. The balloon, considered to be a fully inflated rigid sphere, is modeled as a point mass and constitutes point mass number $N+1$ of the lower tether. The attitude of the gondola G is stabilized by a set of three reaction wheels, W_1, W_2, and W_3, located at the center of mass of G. Their spin axes are directed along the principal axes of G. The camera C is connected to G through a universal joint, allowing two rotational degrees of freedom (θ and ϕ) for the relative

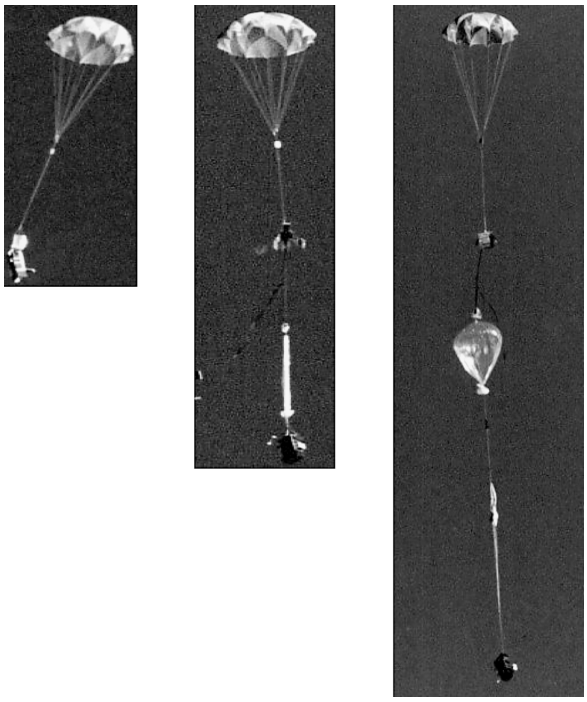

Fig. 1 Flight test of 3-m Mylar balloon.[1]

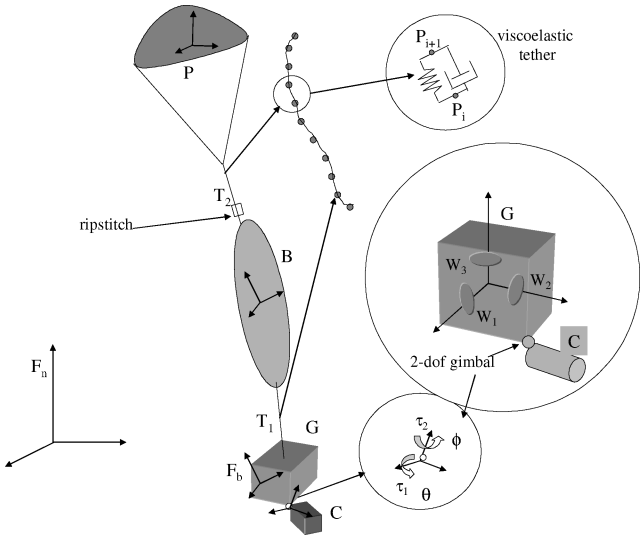

Fig. 3 Multibody model of the system used in the simulation; model components are parachute, balloon, gondola, camera, reaction wheels, and tethers.

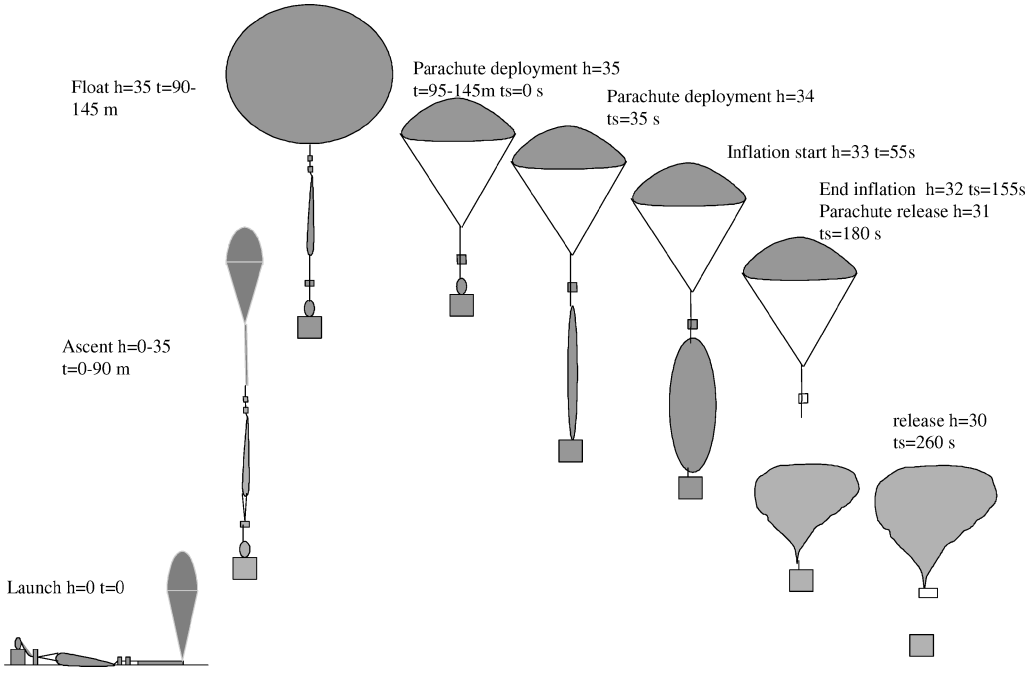

Fig. 2 Sequence of events in the planned stratospheric tests on Earth (numbers refer to some of the tested flights).

motion of C with respect to G. The balloon is subject to gravity and to a constant flow of air in the $\boldsymbol{i}_3$ direction. Partial inflation of the envelope is very difficult to model because it implies a deformable envelope, and so we assume the balloon is 100% full. However, the gas inside the envelope is a partial mixture of the percentage of helium a_{He} and of the percentage of air a_{air}. Given the gas constants of He and air [$R_{\mathrm{He}} = R_0/\mu_{\mathrm{He}} = 2077.15$ J/(kg · K) and $R_{\mathrm{air}} = R_0/\mu_{\mathrm{air}} = 286.06$ J/(kg · K), where the molecular weights are $\mu_{\mathrm{He}} = 4.003$ and $\mu_{\mathrm{air}} = 28.97$ and $R_0 = 8314$ J/(kg · K)], the densities are given by the equations $\rho_{\mathrm{He}} = p_0/R_{\mathrm{He}}T_0$ and $\rho_{\mathrm{air}} = p_0/R_{\mathrm{air}}T_0$, and the masses are given by $M_{\mathrm{He}} = a_{\mathrm{He}}V\rho_{\mathrm{He}}$ and by $M_{\mathrm{air}} = (1 - a_{\mathrm{He}})V\rho_{\mathrm{air}}$, where V is the volume of the balloon sphere and the total mass of gas inside the envelope is $M_{\mathrm{He}} + M_{\mathrm{air}}$. If M_{env} is the mass of the material of the envelope, and M_{added} is the added mass of air caused by the fact that the balloon moves in a fluid, we have the total balloon mass being $M_{\mathrm{tot}} = M_{\mathrm{He}} + M_{\mathrm{air}} + M_{\mathrm{env}} + M_{\mathrm{added}}$, where the added mass is $M_{\mathrm{added}} = 0.5\rho_{\mathrm{air}}V$ for a sphere immersed in a fluid. The buoyancy vector is given by $B = [\rho V g - (M_{\mathrm{He}} + M_{\mathrm{air}})g]\boldsymbol{i}_3$. The drag on the balloon is represented by $D_b = 1/2\rho_{\mathrm{air}}V_b^2 C\, D_b S_b$ with drag coefficient $C_{D_b} = 0.4$, balloon frontal area S_b, and center of mass velocity equal to $V_b = \sqrt{[(\dot{x}_b - U_x)^2 + (\dot{y}_b - U_y)^2 + (\dot{z}_b - U_z)^2]}$, where U_i is the (absolute) component of the airflow in the ith direction. We assume that there is no lift force acting on the balloon, only drag and buoyancy forces. However, an unsteady force acts on the balloon perpendicular to the direction of the relative flow and is caused by the vortex detachment behind the balloon. It is given by $S_b = \frac{1}{2}\rho_{\mathrm{air}}V_b^2 C\, D_b S_b \sin(2\pi\nu t)$, where $Sr = \nu D_b/V$ is the Strouhal number.[8] For the spherical balloon, $Sr = 0.2$. The sinusoidal term is the simplest representation of the unsteady behavior, which, in a more realistic model, would contain higher harmonics and would be much more difficult to model. The parachute is modeled as a rigid body with added mass and inertia. The aerodynamic coefficients of the parachute involve a normal, tangential, and pitching moment coefficient as a function of parachute angle of attack. A cross parachute was used in the tests, and the coefficients of a commercial cross parachute were used in the simulations.[9–11]

B. System Equations of Motion

We adopt a projection method (as in Ref. 12) to derive the equations of motion for a general multibody system composed of one parachute, one balloon (possibly of changing size on account of the inflation process), one gondola (containing three independently articulated reaction wheels and a gimbaled camera), and a deformable tether discretized into a number of lumped masses. This method leads to a set of equations that are easily coded in symbolic form, and they are all written in terms of the velocities. The total number of bodies forming the gondola–camera–wheels–tether–balloon–tether–parachute system is $n_{\mathrm{bod}} = 6 + 3 + 2 + N_p + 3$, where N_p is the number of tether points (inclusive of the balloon) with one extra node for the parachute. There are six degrees of freedom for the gondola, three for the reaction wheels (one per wheel), two for the articulation angles of the gimbal, three for the parachute, and N_p for the remaining nodes forming the tether. From the lowest point, first the gondola (rigid body 1) is connected to the camera (rigid body 2). The gondola is connected at H_1 to the first lower tether node (mass point). The last lower tether node (mass point) is connected to the balloon (mass point). The balloon is connected to the upper riser (upper tether mass points). The last upper riser node is connected to the parachute (mass point). For the sake of brevity, in the following equations we describe the dynamics of the system excluding the parachute and the upper riser, that is, assuming the parachute has already been detached and that the balloon is at float altitude. The total number of configuration degrees of freedom (DOF) is $nq = 7 + 3 + 2 + 3 \cdot N_p + 3$, where the attitude of the gondola is parameterized in terms of the quaternion vector, with four components. There are seven parameters describing the position and the attitude of the gondola, one rotational angle for each wheel (three DOF), two articulation angles for the camera, three position DOF for the tether nodes, and three components of the position of the parachute. The total number of velocity DOF is $n_{\mathrm{speed}} = 6 + 2 + 3 + 3 \cdot N_p + 3$, one less than the number of the configuration parameters because the angular velocity of the gondola is represented by three vector components. We, therefore, identify the following generalized velocities for the problem: $\dot{x}$, $\dot{y}$, $\dot{z}$, ω_1, ω_2, ω_3, Ω_1, Ω_2, Ω_3, $\dot{\theta}$, $\dot{\phi}$, $\dot{x}_1$, $\dot{y}_1$, $\dot{z}_1$, $\dot{x}_2$, $\dot{y}_2$, $\dot{z}_2$, …, $\dot{x}_N$, $\dot{y}_N$, $\dot{z}_N$, $\dot{x}_{N+1}$, $\dot{y}_{N+1}$, and $\dot{z}_{N+1}$. A subindexed speed denotes a kinetic velocity. (For instance, ${}^N\boldsymbol{e}_k^{G+}$ represents the partial derivative of ${}^N\boldsymbol{v}^{G+}$ in the direction of the kth generalized velocity, as described in Refs. 12 and 13.) From the preceding information about the system's topology and kinematics, we obtain the generalized kinetic velocities ${}^N\boldsymbol{e}_k^{G+}$, ${}^N\boldsymbol{e}_k^{Q}$, ${}^N\boldsymbol{e}_k^{H1}$, ${}^N\boldsymbol{e}_k^{P+}$, ${}^N\boldsymbol{e}_k^{i}$, ${}^N\boldsymbol{\eta}_k^{G}$, ${}^N\boldsymbol{\eta}_k^{W_1}$, ${}^N\boldsymbol{\eta}_k^{W_2}$, ${}^N\boldsymbol{\eta}_k^{W_3}$, and ${}^N\boldsymbol{\eta}_k^{P}$, where $k = 1, \ldots, 11 + i + 2$, and $i = 1, \ldots, N_p$. These velocities represent the projection of the translational velocity of each point $\boldsymbol{e}$ and angular velocity of rigid body $\boldsymbol{\eta}$ along the direction of the motion allowed by the constraints acting on the system. For body $\boldsymbol{G}$, and denoting by $\boldsymbol{q}$ the vector of generalized coordinates and by δ a virtual variation, one has $\delta\,{}^N\boldsymbol{r}^{G+} = {}^N\boldsymbol{e}_k^{G+}\delta\boldsymbol{q}_k$ and $\delta\,{}^N\boldsymbol{\omega}^{G} = {}^N\boldsymbol{\eta}_k^{G+}\delta\boldsymbol{q}_k$. For this application, we are only dealing with holonomic constraints and a chain topology, for which the formulation being used is well suited.[13] Consequently, the vector of internal forces and torques, namely, the vector of inertial, Coriolis, and centrifugal forces (that is, the left-hand side of the equations of motion) can be written as follows:

$$
\begin{aligned}
\boldsymbol{G}_k^{\mathrm{internal}} = {} & \left(m_G + \sum_i^3 m_{W_i}\right){}^N\boldsymbol{a}^{G+} \cdot {}^N\boldsymbol{e}_k^{G+} + m_P\,{}^N\boldsymbol{a}^{P+} \cdot {}^N\boldsymbol{e}_k^{P+} \\
& + \sum_i^{N_P} m_i\,{}^N\boldsymbol{a}^{i} \cdot {}^N\boldsymbol{e}_k^{i} + {}^N\boldsymbol{\eta}_k^{P} \cdot \left(\boldsymbol{J}_P\,{}^N\boldsymbol{\alpha}^{P} + {}^N\boldsymbol{\omega}^{G} \times \boldsymbol{J}_P\,{}^N\boldsymbol{\omega}^{P}\right) \\
& + \sum_i^3 {}^G\boldsymbol{\eta}_k^{W_i} \cdot \left[\boldsymbol{J}_i({}^N\boldsymbol{\alpha}^{G} + {}^N\dot{\boldsymbol{\Omega}}^{W_i}) + {}^N\boldsymbol{\omega}^{G} \times \boldsymbol{J}_i({}^N\boldsymbol{\omega}^{G} + {}^G\boldsymbol{\omega}^{W_i})\right] \\
& + {}^N\boldsymbol{\eta}_k^{G} \cdot \left\{\left(\boldsymbol{J}_G + \sum_i^3 \boldsymbol{J}_i\right){}^N\boldsymbol{\alpha}^{G}\right\} \\
& + {}^N\boldsymbol{\eta}_k^{G} \cdot \left\{{}^N\boldsymbol{\omega}^{G} \times \left[\left(\boldsymbol{J}_G + \sum_i^3 \boldsymbol{J}_i\right){}^N\boldsymbol{\omega}^{G}\right]\right\} \\
& + {}^N\boldsymbol{\eta}_k^{G} \cdot \left\{\sum_i^3 \left[\left(\boldsymbol{J}_i\,{}^G\dot{\boldsymbol{\Omega}}^{i} + {}^N\boldsymbol{\omega}^{G} \times \boldsymbol{J}_i\,{}^G\boldsymbol{\Omega}^{i}\right)\right]\right\} \qquad (1)
\end{aligned}
$$

from which the system inertia matrix and nonlinear terms can be derived. In sequence, the first three lines represent the contribution of the translation terms of the gondola, camera, and tether points, respectively. The fourth, fifth, and sixth lines represent the contribution of the rotation terms of the camera, gondola, and reaction wheels, respectively. The (rth, sth) entry of the system's inertia matrix is given by

$$
\begin{aligned}
M_{rs} = {} & \left(m_G + \sum_i^3 m_{W_i}\right){}^N\boldsymbol{e}_r^{G+} \cdot {}^N\boldsymbol{e}_s^{G+} + m_P\,{}^N\boldsymbol{e}_r^{P+} \cdot {}^N\boldsymbol{e}_s^{P+} \\
& + \sum_i^{N_P} m_i\,{}^N\boldsymbol{e}_r^{i} \cdot {}^N\boldsymbol{e}_s^{i} + {}^N\boldsymbol{\eta}_r^{P} \cdot \boldsymbol{J}_P\,{}^N\boldsymbol{\eta}_s^{P} \\
& + \sum_i^3 {}^G\boldsymbol{\eta}_r^{W_i} \cdot \left[\boldsymbol{J}_i\left({}^N\boldsymbol{\eta}_s^{G} + {}^G\boldsymbol{\eta}_s^{W_i}\right)\right] \\
& + {}^N\boldsymbol{\eta}_r^{G} \cdot \left\{\left(\boldsymbol{J}_G + \sum_i^3 \boldsymbol{J}_i\right){}^N\boldsymbol{\eta}_s^{G} + \sum_i^3 \boldsymbol{J}_i\,{}^G\boldsymbol{\eta}_s^{W_i}\right\} \qquad (2)
\end{aligned}
$$

where the indices r and s run over the range of the index k.

The vector of generalized external forces can be written in component form when the velocities of each point of force application

and the angular velocity of each frame of reference where a torque is applied are brought into evidence. Denoting within brackets the sum of external forces and moments acting on each body, we obtain a summation in the form

$$\begin{aligned}\boldsymbol{G}_k^{\text{external}} &= (\boldsymbol{W}_g + \boldsymbol{F}_{g_{\text{aero}}}) \cdot {}^N\boldsymbol{e}_k^{G+} + (\boldsymbol{T}_1) \cdot {}^N\boldsymbol{e}_k^{H1} + (\boldsymbol{W}_p) \cdot {}^N\boldsymbol{e}_k^{P+} \\ &+ \sum_i^{Np} \left(\boldsymbol{W}_i + \boldsymbol{F}_{i_{\text{aero}}} + \boldsymbol{T}_i - \boldsymbol{T}_{i-1}\right) \cdot {}^N\boldsymbol{e}_k^i \\ &+ \left(\boldsymbol{W}_{N_p+1} + \boldsymbol{F}_{N_p+1_{\text{aero}}}\right) \cdot {}^N\boldsymbol{e}_k^{N_p+1} + \left(\boldsymbol{B}_b - \boldsymbol{T}_{N_p+1}\right) \cdot {}^N\boldsymbol{e}_k^{N_p+1} \\ &+ (\tau_\phi s\theta, -\tau_\phi c\theta, \tau_\theta)\hat{\boldsymbol{F}}_b \cdot {}^N\boldsymbol{\eta}_k^P + \sum_i^{Nw} (\boldsymbol{\tau}_{wi}) \cdot {}^G\boldsymbol{\eta}_k^{W_i} \\ &+ [-\boldsymbol{\tau}_{w1} - \boldsymbol{\tau}_{w2} - \boldsymbol{\tau}_{w3}] \cdot {}^N\boldsymbol{\eta}_k^G \\ &- [(\tau_\phi s\theta, -\tau_\phi c\theta, \tau_\theta)\hat{\boldsymbol{F}}_b] \cdot {}^N\boldsymbol{\eta}_k^G \end{aligned} \tag{3}$$

where $\boldsymbol{W}_g$, $\boldsymbol{W}_p$, and $\boldsymbol{W}_i$ for $i = 1, \ldots, N_p$ are the weights of each body; and $\boldsymbol{F}_{g_{\text{aero}}}$ and $\boldsymbol{F}_{i_{\text{aero}}}$ are the aerodynamic forces acting on the center of mass of the gondola and ith tether link. (There is also an aerodynamic moment, but it is probably of very small magnitude on a near spherical balloon.) $\boldsymbol{T}_i$ is the tether tension in the ith link; $\boldsymbol{B}_b$ is the balloon buoyancy force; $\boldsymbol{\tau}_{wj}$ for $j = 1, 2, 3$ are the reaction wheel command torques; and $\boldsymbol{\tau}_\theta$ and $\boldsymbol{\tau}_\phi$ are the camera gimbal command torques in the θ and ϕ directions, respectively. The tension in the ith viscoelastic tether segment of length l, strain ε, strain rate $\dot{\varepsilon}$, stiffness coefficient K, and damping coefficient C, is $|\boldsymbol{T}_i| = K\varepsilon + C\dot{\varepsilon}$. It is set to zero if the resultant force is compressive (unilateral spring).

The resulting equations of motion for each degree of freedom k can be written as $\boldsymbol{G}_k^{\text{external}} - \boldsymbol{G}_k^{\text{internal}} = 0$ and have been directly programmed in MATLAB®/Simulink in the form in which they have just been described, resulting in a very compact computer program. The equations of motion have been integrated with the ode15s variable step integrator available in MATLAB[14] because of the presence of discontinuous behavior and tether elasticity, with a tendency to make the system numerically stiff.

III. Ripstitch Constitutive Models

An important modeling element in the MABVAP program was the derivation of low-order models of the ripstitch (shock alleviation device), which can be incorporated in low-order dynamic models of deployment analyses with the intention of correlating the simulated response with laboratory quasi-static tensile tests and with flight data. Fig. 4a represents one of the considered locations of the ripstitch in the flight train. The proposed constitutive model of the ripstitch is based on a zig-zag profile of tension vs displacement difference $dx = x_2 - x_1$ between the upper and lower nodes of the ripstitch, and confined between a minimum ($f_{\min}$) and maximum ($f_{\max}$) force. The length of group of stitches is dx_{stitch}, and $dx_{\max}$ is the maximum length of breakable ripstitch. Figure 4b shows the load-displacement model. A viscous damper is also placed in parallel to introduce some dissipation into the process. Figures 5a and 5b depict two of the models considered: The former involves a ripstitch located below the tether, whereas the latter models the ripstitch between the tether and an infinitely rigid wall at the top. It was observed that the ripstitch response is very dependent on the number of stitches, on the location with respect to the payload, and on the strength of the stitches. The qualitative response of the modeled ripstitch was shown to agree well with quasi-static tests. The parameters

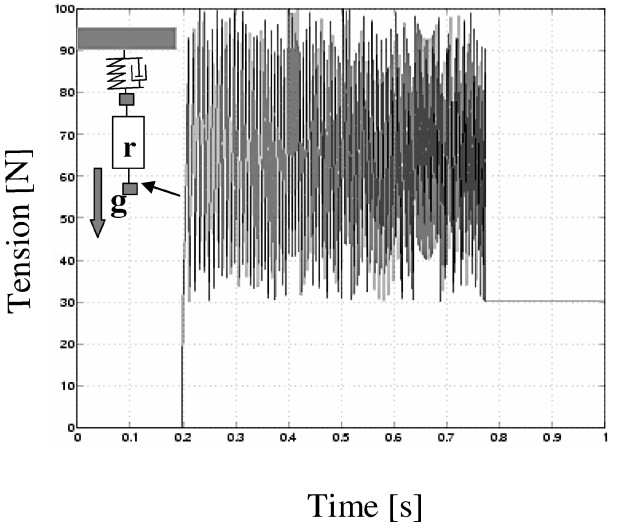

Fig. 5a Tension vs time at bottom of ripstitch in first model.

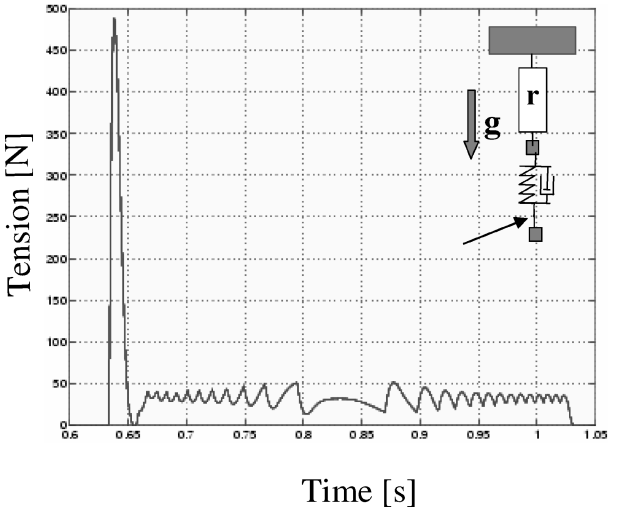

Fig. 5b Tension vs time at bottom of ripstitch in second model.

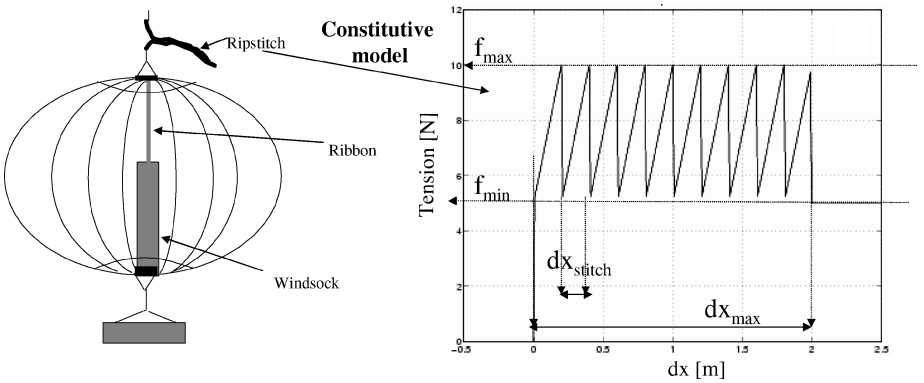

a) b)

Fig. 4 a) Balloon configuration with ripstitch and b) constitutive modeling of ripstitch.

of the constitutive model are very dependent on the construction, but it was felt that the essential features of the ripstitch behavior were captured with these simple models with no internal states.

IV. Wind Models

Only one-dimensional wind data are available from existing models of Martian winds, and these models are stochastic in nature. To generate wind data that are representative of typical planetary winds that a balloon might encounter, we developed a stochastic wind model based on a first-order Markov model. For this model, we assume that the varying winds can be represented in the form $\dot{v}(t) = -\beta v(t) + \sigma_N w(t)$, where $w(t)$ is a zero-mean, unity variance, white noise process with expected value $E[w(t)] = \bar{w}(t) = 0$ and covariance $E[w(t)^2] = 1$. To construct simulated wind data that have similar characteristics to actual wind data, it is necessary to analyze actual data and extract two parameters, the standard deviation of the wind velocity (σ_v), and the autocorrelation time T_v. The meaning of the correlation time is that the wind velocity is not highly autocorrelated beyond much more than the correlation time. Unfortunately, the use of the simple differential equation for the wind noise model in most modern adaptive integrators will produce significant computational thrashing. The reason behind this is that the white noise process $w(t)$ must be approximated by calling a Gaussian random number generator. This means the right-hand side of the preceding governing differential equation will not reproduce the same value as t approaches some specific time (t_k) in the limit because no two samplings of $w(t_k)$ will produce the same number. The wind speed model is, therefore, simulated at discrete time steps, and it is described in discretized form as the result of the application of a simple Euler integration scheme at every time step Δt to the speed W_k in the form:

$$W_{k+1} = W_k - \beta x_k \Delta t + \left(\sqrt{2\beta \Delta t}\big/\sigma_v\right) w_k \tag{4}$$

where w_k is a zero mean, unity variance, randomly generated number, and the parameter β is defined to be the reciprocal of the correlation time ($\beta = 1/T_v$). Although this discrete update equation can be used as part of a user-defined fixed-step integration routine, perhaps a better approach is to use this exact scheme to generate a set of wind data having the desired characteristics. Then, use that synthetic wind data (with associated time information) to construct a function $W(t)$ that will do a table lookup in the earlier generated wind data, interpolate if desired, and return the wind at the specified time. This function can be used directly with adaptive integration routines because the values are reproducible for a specific t_k and approach the same value as t_k is approached from either side. To extract the stochastic parameters σ_v and T_v from available wind data, we assume that we have a set of N wind velocity samples v_i, sampled at time intervals of Δt_v. Getting the standard deviation of the wind velocity requires a simple statistical analysis

$$\sigma_v^2 = \frac{1}{N-1}\sum_{i=1}^{N}(v_i - \bar{v})^2 \tag{5}$$

where $\bar{v}$ is the mean of the wind velocity values. Determining the autocorrelation time, we define the autocorrelation function

$$f(k) = \frac{1}{N-k-1}\sum_{i=1}^{N-k}(v_i - \bar{v})(v_{i+k} - \bar{v}) \tag{6}$$

This function correlates the data with a shifted version of itself in a root-mean-square sense. If $k = 0$, $f(k)$ should reproduce the variance of the data. If $k = 1$, $f(k)$ should give the correlation of the data with the data shifted one time step Δt_v. As k increases, the autocorrelation should decrease exponentially. Applying the autocorrelation function for various k determines how large k has to get for the values of $f(k)$ to be small. Let K be the necessary value of k for $f(k)$ to be as small as desired. Now construct a set of data pairs $[t_k, f(k)]$ from $k = 0$ to K where $t_k = k\Delta t$. The result, when plotted, will produce an autocorrelation plot. To determine the autocorrelation time from the autocorrelation data, it is necessary to fit the data to an exponential function $A\exp(-t_k/T_v)$. The resulting estimate of T_v will be a good approximation of the autocorrelation time, and its reciprocal is the desired β necessary for the wind model.

V. Descent Under Inflating Balloon

A. System Stability

One of the problems requiring investigation was the system stability (residual gondola oscillations) during descent when the parachute is suddenly detached and the balloon is being inflated. The main purpose for conducting this analysis is then to determine the influence of flight-train parameters on overall system stability. The assumptions of the dynamic process are as follows: The parachute (modeled as a point mass) is fully opened, and the aerodynamic flow is steady. The system is descending at terminal velocity. The tethers connecting the balloon to the gondola and the balloon to the parachute are modeled as a chain of masses, and the gondola is modeled as point mass. The balloon inflation process is modeled as a linear increase of the mass of enclosed gas vs time and relies on empirical profiles of mass flow rate vs time. Consequently, the volume of the balloon varies with time until maximum inflation is reached.

The simulation was run on Earth at 1000-m altitude, with a tether 20 m long, a balloon diameter linearly growing from a radius of 0.01 m up to a 12-m radius, a gondola with a mass of 5 kg, a cross parachute of 2-m radius with suspension lines 2 m long, and no wind acting on the system.

Figure 6 depicts the phases of the parachute release, the balloon inflation, and the ensuing gondola oscillation (measured as

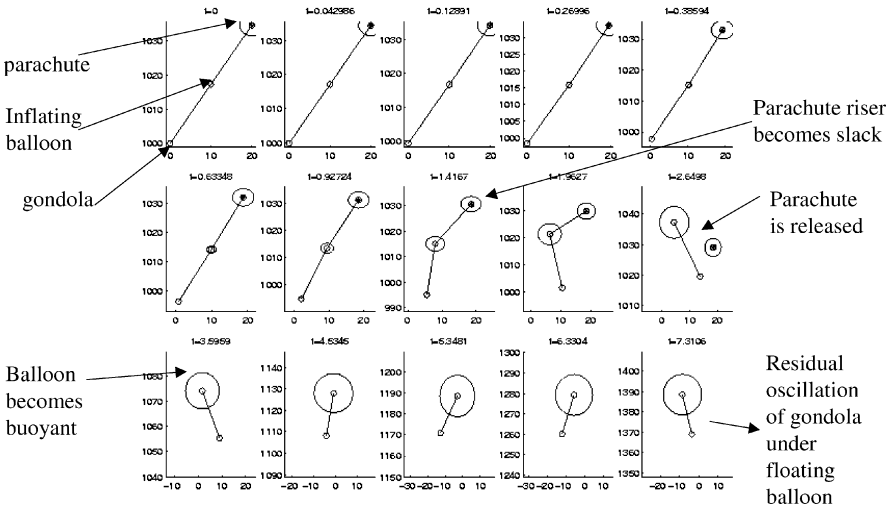

Fig. 6 Snapshots of descent under inflating balloon, with parachute detachment phase; horizontal axis represents the horizontal coordinate x, and the vertical axis represents the vertical coordinate z (both in meters) in each plot.

the angle of the gondola–balloon line vs the fixed vertical inertial direction). Two different inflation profiles are shown in Figs. 7 (inflation duration = 5 s) and 8 (inflation duration = 100 s), where the balloon radius, the residual gondola oscillation, and the tension in the parachute and balloon risers, respectively, are shown vs time.

The oscillatory behavior ensuing after full inflation of the balloon and successive parachute elimination can be seen in Figs. 7 and 8. The link between the balloon and the parachute is cut and remains cut when the first of the following two events is true: 1) The altitude of the balloon equals the altitude of the parachute. 2) The tether tension in that link becomes negative. The link to the parachute is cut because the parachute becomes ineffective as the balloon becomes buoyant, and no drag force is transmitted to the parachute. A dramatic reduction of the gondola oscillation results if the duration of the balloon inflation profile is slow compared to a fast one, as a comparison between Figs. 7 and 8 will show. The tension in the upper and lower links rises quickly from 0N to a maximum value in Figs. 7 and 8. The initial transient

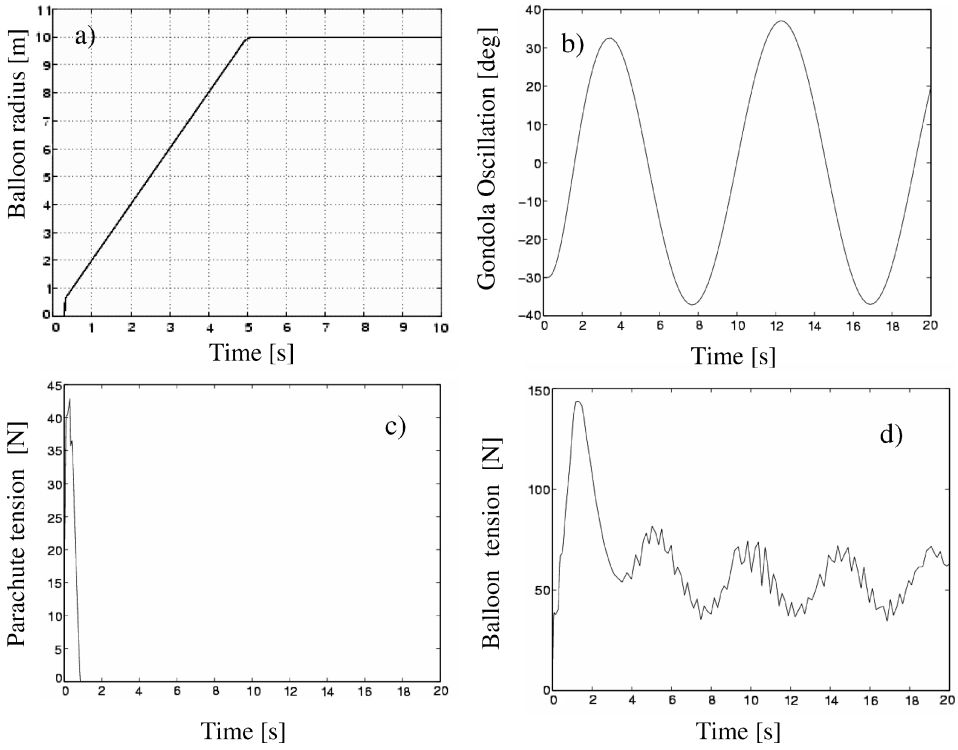

Fig. 7 Simulation with rapid inflation: a) balloon radius vs time, b) residual gondola oscillation vs time, c) tension in parachute riser vs time, and d) tension in parachute–balloon riser vs time.

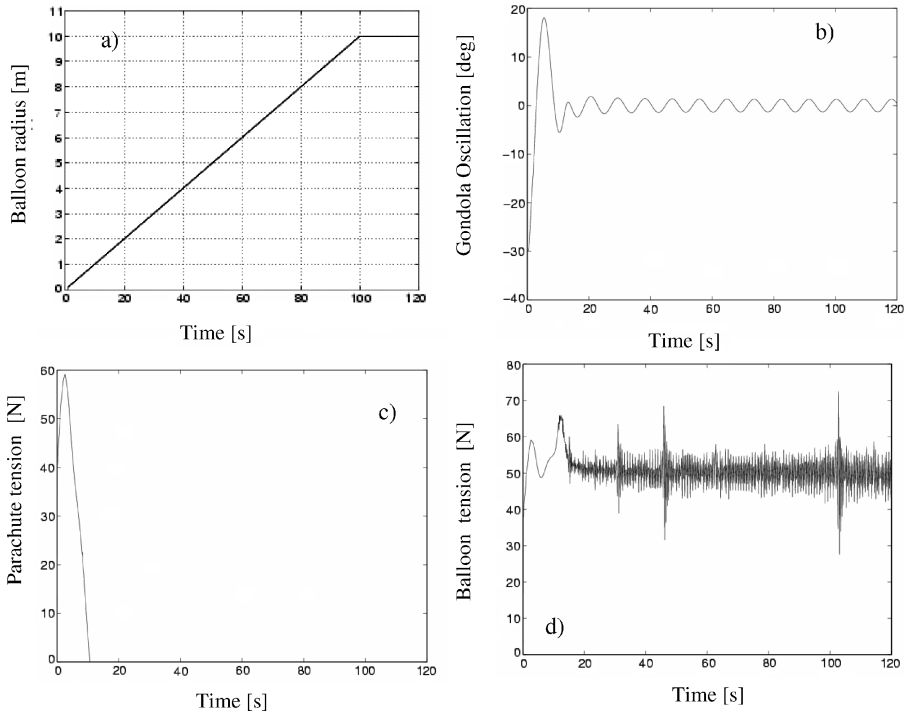

Fig. 8 Simulation with slow inflation: a) balloon radius vs time, b) residual gondola oscillation vs time, c) tension in parachute riser vs time, and d) tension in parachute–balloon riser vs time.

occurs because the simulation is started when the system is released with zero tension in the upper and lower links, after which the system reaches its natural equilibrium. In particular, the tension in the upper link eventually drops to zero because the parachute is detached, whereas the tension in the lower link reaches a steady state with a residual oscillatory behavior, reflecting the pendular motion of the payload.

B. Pointing Control Algorithms

Once the parachute has been released, the balloon reaches a floating altitude, and the problem becomes quantifying the performance of the pointing algorithm that autonomously controls the camera boresight to follow a specified target on the ground while perturbations (such as a wind gust) act on the system. Figure 3 shows the model of the system being simulated. The actuators considered are a set of three reaction wheels, of sizes consistent with those used in scientific ballooning experiments. The reaction wheels operate about the nominal attitude of the gondola and provide three-axis stabilization of the reference body triad from which the pointing payload (camera) operates. The payload is hinged at a bottom location on the gondola, via a universal-joint connection, or a two-DOF gimbal. This implies that there are two independent axes that need to be controlled to provide declination and azimuth of the payload about the reference body triad represented by the gondola body axes. With the dynamics described earlier, that is, payload and gondola dynamics, reaction wheel dynamics, and balloon and tether dynamics, the equations of motion are strongly coupled through centrifugal and Coriolis terms (gyroscopic forces). These forces are of small magnitude if sufficiently slow maneuvers take place and provided that the attitude of the gondola is only slightly perturbed from an equilibrium inertial orientation.

Therefore, with standard sensing equipment located onboard the gondola, that is, three-axis accelerometers, gyro unit, and a global attitude determination system such as an onboard star tracker, inertial position (in planetocentric coordinates), inertial attitude (with respect to the planetocentric reference frame, which is being propagated through ephemeris in the onboard computer), and their rates can be determined. Some estimation procedure is necessary when the full dynamic state cannot be measured. With this information, the nonlinear gyroscopic terms can be canceled from the equations. This results in a feedback linearized equation of motion in the direction of the controlled axes, namely, we achieve near-perfect state decoupling, and we can design the local controllers assuming independent control loops.

The pointing control algorithms developed for this study rely on a feedback linearization of the dynamics to derive a globally, exponentially stable controller for the pointing dynamics. An attitude estimator onboard the gondola provides real-time estimates of the attitude quaternion and angular velocity. A command profiler specifies the command to be tracked, in the form of a constant or a step vs time. These commands are provided to the controller in the form of desired attitude, angular velocity, and angular acceleration. It is desired to cancel all possible dynamic nonlinearities arising from gyroscopic and centrifugal terms, as derived from Eq. (1). The rotational control torque vector $\boldsymbol{\tau}$ is of the following form

$$\boldsymbol{\tau} = \boldsymbol{\Gamma}_{pi}[\boldsymbol{\lambda}(\theta_{\text{err}})_{\text{cmd}} - \boldsymbol{\lambda}(\theta_{\text{err}})_{\text{est}}] + \boldsymbol{\Gamma}_{vi}\left({}^{N}\boldsymbol{\omega}^{P}_{\text{cmd}} - {}^{N}\boldsymbol{\omega}^{P}_{\text{est}}\right) + \boldsymbol{J}_P\,{}^{N}\boldsymbol{\alpha}^{P}_{\text{cmd}} + \boldsymbol{h}_{\text{cancel}} \tag{7}$$

where $\boldsymbol{\Gamma}_{pi}$ and $\boldsymbol{\Gamma}_{vi}$ are rotational control gain matrices; $\boldsymbol{J}_P$ is the camera moment of inertia matrix; λ is the unit eigenaxis of rotation; θ_{err} is the magnitude of rotation corresponding to the difference between the commanded and the estimated quaternion; $\boldsymbol{h}_{\text{cancel}}$ is the vector of the centrifugal and Coriolis nonlinear terms to be canceled, which can be obtained from the appropriate terms in Eq. (1); and ${}^{N}\boldsymbol{\omega}^{P}$ and ${}^{N}\boldsymbol{\alpha}^{P}$ are the angular velocity and acceleration vectors of the camera, respectively. Based on the inertia of the gondola (a cubical body of moment of inertia equal to approximately 1 kgm^2), the gains were selected to be $\boldsymbol{\Gamma}_{pi} = 40.2680$ Nm/rad and $\boldsymbol{\Gamma}_{vi} = 12.8177$ Nms/rad to ensure a stable and critically damped response. The desired inertial angle, measured as the sum of the angle of the camera with respect to the gondola in the vertical plane plus the gondola angle in the x–z plane, is -10 deg.

The simulation was run for a tether with three links, a gondola mass of 10 kg and moment of inertia of 1 kgm^2, a camera of 0.3 kg, a balloon mass of 62.21 kg and a diameter of 22.2 m, tether lengths varying from 5 to 100 m, and wind speeds ranging from 1 up to 50 m/s.

The simulation used the ode15 s integrator for the same reasons it was used in the simulations described earlier, that is, capability of handling discontinuous behavior and numerical stiffness. Figure 9a shows the pointing error of the gondola instrument (inertial angular error) vs time during a 20-m/s lateral wind gust of 2-s duration in the X direction for a tether length of 5 m. The pointing angle remains bounded to within 0.5 arcs after the wind gust has acted. Figure 9b shows the tether tension in Newtons in the first tether link above the gondola. These results are useful in identifying the issues affecting gondola stability and the effects of wind changes that affect the pointing performance. Also, when the tether tension is monitored it is possible to get some insight into the possible failure modes of the flight train because the balloon is the weakest link on account of the light material of which it is made. Figure 10a shows the camera inertial angle vs time with a wind gust of 10 m/s, for a tether length of 5 and 100 m. Figure 10b shows the camera inertial angle vs time for a fixed tether length of 100 m, when the wind gust changes from 1 to 10 m/s. As a general trend, after the onset of the wind gust, the system reaches an oscillatory state that remains bounded and does not affect the pointing performance of

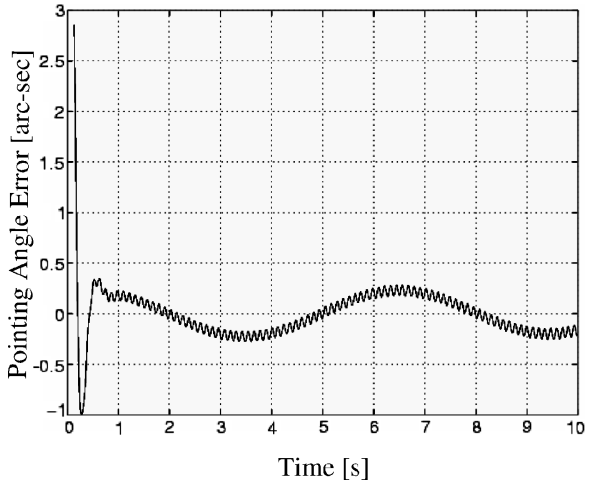

Fig. 9a Camera pointing error (arcseconds) vs time.

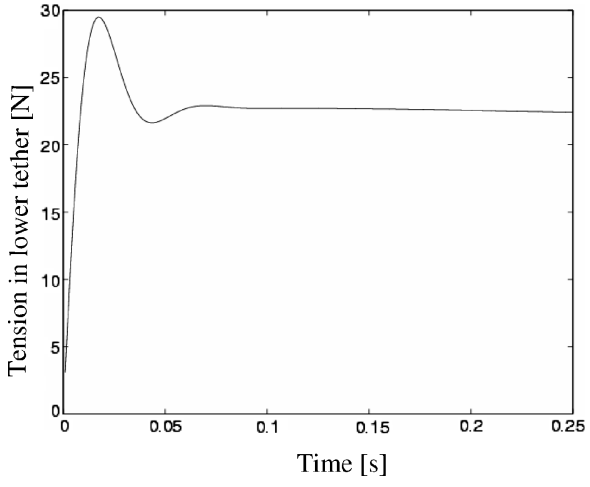

Fig. 9b Tension in lower tether (Newtons) vs time.

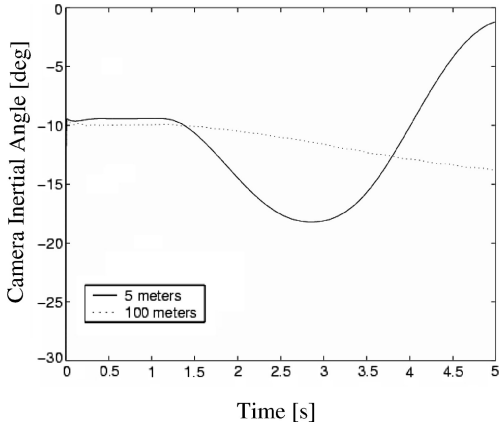

Fig. 10a Camera inertial angle vs time with a wind gust of 10 m/s, for a tether length of 5 and 100 m.

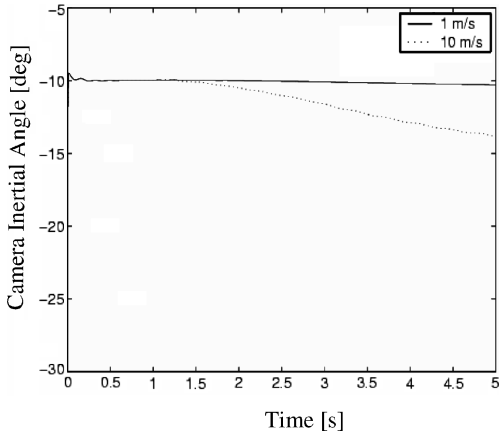

Fig. 10b Camera inertial angle vs time for a fixed tether length of 100 m, when the wind gust changes from 1 to 10 m/s.

the instrument. The general trend is that the longer the length of the tether connecting the gondola and the balloon, the smaller the oscillations of the system. However, and depending of the wind intensity and duration, the oscillations can grow larger and take a longer time to subside for a system with a long tether compared to a short one.

VI. Conclusions

In this paper, we have documented the analysis done to assess the validity of models developed for parachute and balloon-assisted deployment of sensor packages within the Mars Aerobot Validation program at the Jet Propulsion Laboratory, California Institute of Technology. These models have been motivated by the need to predict and validate flight-train stability behavior on deployment before and after tests have been made. First, we have described models of the descent of the system while the parachute is detached and the balloon inflates, with the intent of observing the stability of the system and identifying possible failure modes. Models of the shock alleviation mechanism that mitigates the deployment shock have also been described. The result of the simulations confirms that a slow balloon inflation profile is very beneficial in reducing gondola oscillations. Second, using the same models, we have simulated the pointing dynamics of a hinged camera onboard the gondola while a lateral wind gust acts on the system, showing that a set of reaction wheels with a feedback linearizing controller succeeds in stabilizing the gondola in the arcsecond range after the wind gust acts.

Acknowledgments

This research was carried out at the Jet Propulsion Laboratory, California Institute of Technology, under a contract with NASA. The authors are grateful to J. Cutts, F. Hadaegh, and J. Hall for helpful suggestions.

References

[1]Kerzhanovich, V. V., Cutts, J., Bachelder, A., Cameron, J., Hall, J., Patzold, J., Yavrouian, A., Cantrell, J., and Lachenmeier, T., "Mars Aerobot Validation Program," *Proceedings of the AIAA International Balloon Technology Conference*, AIAA, Reston, VA, 1999, pp. 8–20.

[2]Quadrelli, M., Cameron, J., and Kerzhanovich, V., "Modeling, Simulation, and Control of Parachute/Balloon Flight Systems for Mars Exploration," AIAA Paper 2001-2026, May 2001.

[3]Kerzhanovich, V. V., Cutts, J. A., Bachelder, A. D., Cameron, J. M., Hall, J. L., Quadrelli, B. M., Patzold, J. D., Yavrouian, A. H., Cantrell, J. A., and Lachenmeier, T. T., "MABVAP—One Step Closer to an Aerobot Mission to Mars," 5th International Conference on Mars, Paper 16, The Lunar and Planetary Inst., July 1999.

[4]Ash, R., "Balloon Concepts for Scientific Investigation of Mars and Jupiter," *Proceedings of the AIAA 6th Aerodynamic Decelerator and Balloon Technology Conference*, AIAA, New York, 1979, pp. 26–37.

[5]Carten, A., and Wuest, M., "The Air-Launched Balloon System Phase II Design Improvement and Test Program," 7th AIAA Aerodynamic Decelerator Systems Technology Conference, AIAA Paper 81-1930, 1981.

[6]Romero, M., Rougerch, M., and Tockert, C., "Thermal Balance of Pumpkin Shaped Balloons and Its Relation with IR Earth Radiation," 7th AIAA Aerodynamic Decelerator Systems Technology Conference, AIAA Paper 81-1938, 1981.

[7]Vargas, A., Tarrieu, C., Lepage, J. P., Mauoy, P., and Sirmain, C., "Mars Balloon Simulator," Paper 91-436, International Astronautical Federation Conf., Oct. 1991.

[8]Dowell, E. H. (ed.), *A Modern Course in Aeroelasticity*, 3rd ed., Kluwer Academic Publishers, Norwell, MA, 1995, Chap. 6.1.

[9]Cockrell, D. J., and Young, A. D., *Aerodynamics of Parachutes*, AGARDograph 295, AGARD, 1987.

[10]Ewing, E. G., Bixby, H. W., and Knacke, T. W., "Recovery System Design Guide," Air Force Flight Dynamics Lab., AFDL-TR-78-151, Dec. 1978.

[11]Knacke, T. W., *Parachute Recovery Systems Design Manual*, Naval Warfare Center, NWC TP-6575, March 1992.

[12]Kurdila, A., "Multibody Dynamics Formulations Using Maggi's Approach," *Mechanics and Control of Large Space Structures*, edited by J. L. Junkins, Progress in Aeronautics and Astronautics Series, Vol. 129, AIAA, Washington, DC, 1990, Chap. 6.

[13]Neimark, J. I., and Fufaev, N. A., *Dynamics of Nonholonomic Systems*, American Mathematical Society, Mathematical Monograph 33, Providence, RI, 1972, Chap. 4.

[14]MATLAB, ver. 5.3, The Mathworks, Inc., Natick, MA, 1999.